

## Ultrafast carrier dynamics and symmetry reduction in bismuth by nonperturbative optical excitation in the terahertz range

Matthias Runge<sup>1,\*</sup>, Ahmed Ghalgaoui<sup>1,†</sup>, Isabel Gonzalez-Vallejo<sup>1</sup>, Fabian Thiemann<sup>2</sup>, Michael Horn-von Hoegen<sup>2</sup>, Klaus Reimann<sup>1</sup>, Michael Woerner<sup>1</sup>, and Thomas Elsaesser<sup>1</sup>

<sup>1</sup>Max-Born-Institute for Nonlinear Optics and Short Pulse Spectroscopy, Max-Born-Straße 2A, 12489 Berlin, Germany

<sup>2</sup>Department of Physics and Center of Nanointegration CENIDE, University of Duisburg-Essen, Lotharstraße 1, 47057 Duisburg, Germany



(Received 31 March 2023; accepted 2 June 2023; published 28 June 2023)

The nonlinear optical response of bismuth (Bi) in the nonperturbative regime is studied by phase-resolved two-dimensional terahertz (THz) spectroscopy. A (111)-oriented rhombohedral Bi film of 45-nm thickness is excited by a pair of THz pulses with center frequencies of 1.1 THz, electric field amplitudes of 300 and 600 kV/cm, and pulse durations of 1 ps. The phase-resolved nonlinear signal field, emitted by the sample and recorded in a transmission geometry, allows for a separation of different components of the total nonlinear response, including higher harmonics of the THz pulses and pump-probe signals with few-picosecond decay times. The pump-probe signals originate from irreversible electron-hole pair generation and display a sixfold amplitude pattern in the azimuthal sample orientation. The linearly polarized pump pulses generate an unequal transient carrier population in the six  $L$  valleys of the band structure, resulting in a reduction of symmetry of the excited crystal and a backfolding of phonons from the  $X$  to the  $\Gamma$  point. Wave packets of back-folded acoustic phonons, which are displacively excited by the THz pump pulse, give rise to coherent pump-probe signals oscillating with a frequency of 0.8 THz.

DOI: [10.1103/PhysRevB.107.245140](https://doi.org/10.1103/PhysRevB.107.245140)

### I. INTRODUCTION

The regime of nonperturbative light-matter interaction is characterized by a coupling of electrons to light with electric fields comparable to or even exceeding the interaction strength of charges and elementary excitations in condensed matter. Phenomena such as high-field and ballistic transport [1–3], interband tunneling [4,5], and high-harmonic generation [6–8] of an optical pulse have been induced by strong light fields in a wide range of materials, including semiconductors and semimetals. Of particular interest are processes in which quantum coherence of the material excitation allows for exploring new regimes of carrier dynamics and optical frequency conversion. From the viewpoint of nonlinear optics, nonperturbative light-matter interaction is characterized by a simultaneous occurrence of processes of different nonlinear order in the driving electric field. In most experiments, ultrashort optical pulses with a high peak field and frequencies from the terahertz (THz) to ultraviolet range have been applied for studying nonperturbative interactions.

Recently, quasi-two-dimensional quantum materials such as graphene, hexagonal boron nitride, and dichalcogenides have attracted much interest for their peculiar electronic and optical properties [9–11]. The nonperturbative interaction of graphene with optical or high-field THz pulses has been exploited to generate coherent intra- and interband currents

around the  $K$  and  $K'$  points with their conelike band structure in  $k$  space [12–14]. The currents give rise to the emission of higher harmonics of the driving THz field [13,15], while interband carrier-wave Rabi flopping is facilitated by the extremely large interband transition dipole [16].

The prototypical semimetal bismuth (Bi) exhibits a conelike band structure around the six  $L$  points of its three-dimensional Brillouin zone with a band gap of only  $E_g^L = 15$  meV [ $\nu = E_g^L/h = 3.62$  THz, Fig. 1(a)]. In analogy to graphene, the interband transition dipoles diverge for  $\nu \rightarrow 0$ , resulting in a high Rabi frequency for moderate THz electric fields. While coherent optical phonon excitations [17–24] and, to lesser extent, carrier dynamics [25] have been studied after excitation with femtosecond pulses at photon energies of some 1.5 eV, the transient behavior of electrons close to the  $L$  points, their coupling to phonons and, in particular, nonperturbative light-matter interactions in the THz frequency range are not understood. Phase-resolved nonlinear THz spectroscopy holds a particular potential for new insight in such processes.

In this article, we study ultrafast carrier dynamics in Bi, driven by THz pulses in the nonperturbative regime of light-matter interaction. We employ two-dimensional THz (2D-THz) spectroscopy for a spectral and temporal separation of different interaction pathways and nonlinear signal contributions, such as pump-probe signals and high-harmonic generation up to the fifth harmonic of the THz fundamental. Excitation with linearly polarized THz pulses induces a transient reduction of the azimuthal angular symmetry of the band structure, resulting in an unequal population of  $L$  valleys

\*runge@mbi-berlin.de

†Present address: Department of Physics, TU Dortmund, 44221 Dortmund, Germany.

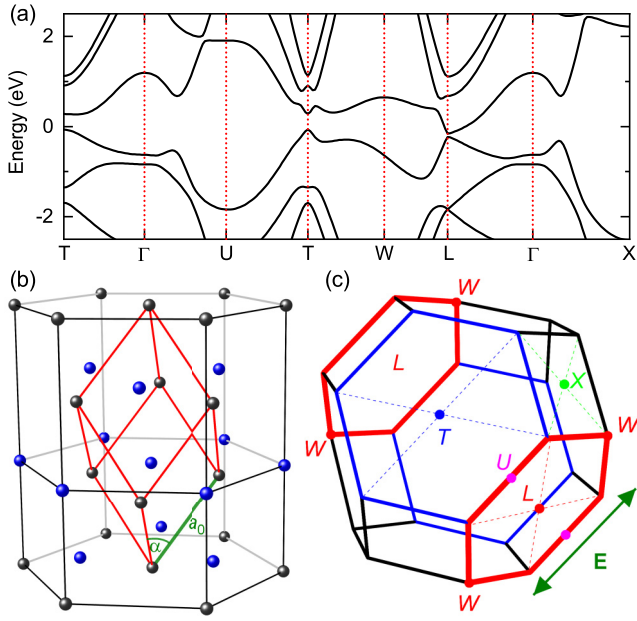


FIG. 1. (a) Electronic band structure of Bi calculated with the density functional theory (DFT) code FLEUR with the local density approximation (LDA) for the exchange-correlation functional [27,28]. A detailed discussion of the band structure around  $L$  is given in Appendix A. (b) Rhombohedral crystal lattice of Bi defined by the length of rhombohedral vectors  $a_0$ , and the angle  $\alpha$ . The dark gray and the blue spheres indicate the two atoms per elementary cell. (c) Schematic of the Brillouin zone. The  $L$  points are positioned in the center of the hexagonal side facets. Red hexagons indicate  $L$  points excited in  $W-L-W$  direction when applying a correspondingly polarized electric field (green double arrow).

by electron-hole pairs. The symmetry breaking leads to a backfolding of phonons from the  $X$  to the  $\Gamma$  point in  $k$  space. This is evident from coherent phonon oscillations observed at a frequency of 0.8 THz. The experimental findings are in line with a theoretical analysis.

## II. CRYSTAL STRUCTURE AND BRILLOUIN ZONE OF BISMUTH

Bi crystallizes in the A7 structure, which can be derived from the simple cubic structure by the application of two separate distortions, a rhombohedral shear and a relative displacement along the  $[111]$  direction of the two fcc sublattices towards each other. The resulting lattice has a trigonal symmetry and contains two atoms per primitive unit cell [Fig. 1(b)]. It is defined by the vectors  $a_0 = 4.7236 \text{ \AA}$ , the angle  $\alpha = 57.35^\circ$ , and an internal displacement factor  $u = 0.234$  [26]. The lattice distortions result in energy gaps opening at the  $L$  and  $T$  points in the Brillouin zone [Fig. 1(a)] with respective band gaps of  $E_g^T = 350 \text{ meV}$  and  $E_g^L = 15 \text{ meV}$  [27]. The lowest conduction band at the  $L$  point overlaps in energy with the highest valence band at the  $T$  point, making Bi semimetallic, i.e., the conduction band in the vicinity of the  $L$  point is populated with electrons up to the Fermi energy.

Figure 1(c) shows the first Brillouin zone of Bi, with the  $T$  points on the hexagonal top and bottom facets, and the  $L$  points on the six quasihexagonal side facets. The green

double arrow indicates an incident THz electric field in orthogonal direction to the  $(111)$  symmetry axis.

## III. EXPERIMENT AND RESULTS

In the experiments we employ 2D-THz spectroscopy [29] to study a  $(111)$ -oriented 45-nm-thick single-crystalline Bi film, epitaxially grown on a  $(111)$ -oriented silicon substrate of 525- $\mu\text{m}$  thickness [30,31]. THz pulses centered at 1.1 THz with durations of approximately 1 ps are generated by optical rectification of 800-nm pulses in a 1.3 mol% MgO-doped stoichiometric LiNbO<sub>3</sub> crystal using tilted wave-front excitation [32]. A gold-coated diamond beamsplitter [33] generates pairs of THz pulses A and B with peak electric fields of 300 and 600 kV/cm, respectively [Fig. 2(a)]. A delay stage allows for tuning the time delay  $\tau$  of pulse A relative to pulse B. The pulses are focused by an off-axis parabolic mirror (effective focal length 25.4 mm) onto the sample. The transmitted THz electric field is recorded as a function of real time  $t$  by free-space electro-optic sampling [Fig. 2(a)]. Two optical chopper wheels with respective frequencies of 250 and 500 Hz allow for separately measuring the transmitted electric-field transients  $E_{AB}(t, \tau)$  of both pulses A and B,  $E_A(t, \tau)$  of only pulse A, and  $E_B(t)$  of only pulse B. The nonlinear THz electric field emitted by nonlinear current densities in the Bi film is given by  $E_{NL}(t, \tau) = E_{AB}(t, \tau) - E_A(t, \tau) - E_B(t)$ . More experimental details of 2D-THz spectroscopy can be found in Ref. [29]. Measurements were performed for different azimuthal angles  $\phi$  of the sample relative to the plane of incidence of the THz pulses.

Figure 2 summarizes the results of the 2D-THz experiments. In Fig. 2(b),  $E_{AB}(t, \tau)$  is plotted as a function of real time  $t$  and delay time  $\tau$ . Figure 2(c) displays the nonlinearly emitted electric field  $E_{NL}(t, \tau)$ . A 2D Fourier transform of  $E_{NL}(t, \tau)$  gives the nonlinear electric field  $E_{NL}(\nu_t, \nu_\tau)$  in frequency space as a function of detection frequency  $\nu_t$  and excitation frequency  $\nu_\tau$ , as shown in Fig. 2(d).  $E_{NL}(\nu_t, \nu_\tau)$  comprises contributions from different types of third-order and higher-order nonlinear responses, including a B-pump-A-probe signal at  $(\nu_t, \nu_\tau) = (1.5, -1.5)$  THz (cf. Fig. 3), signals from third- and fifth-harmonic generation at  $(\nu_t, \nu_\tau) = (3.3, 0)$  THz, and  $(\nu_t, \nu_\tau) = (5.5, 0)$  THz [cf. Fig. 4], an A-B-B four-wave-mixing signal at  $(\nu_t, \nu_\tau) = (1.5, 1.5)$  THz, and an A-pump-B-probe signal at  $(\nu_t, \nu_\tau) = (1.5, 0)$  THz [cf. Fig. 5]. The A-pump-B-probe signal interferes with another signal at  $(\nu_t, \nu_\tau) = (1.2, -0.8)$  THz, which arises from phonons back-folded from the  $X$  to the  $\Gamma$  point, as we will discuss later. The four-wave-mixing signal is limited to the temporal pulse overlap of pulses A and B, suggesting a dephasing time substantially smaller than the pulse duration.

To analyze the nonlinear signal, the change of transmission as a function of the delay time  $\tau$  and the azimuthal angle  $\phi$  is obtained from  $E_{NL}(t, \tau, \phi)$  [Fig. 2(c) for  $\phi = 0$ ] and the THz probe pulse  $E_{Pr}(t, \tau) = E_A(t, \tau)$  using

$$\frac{\Delta T}{T_0}(\tau, \phi) \approx \frac{2 \int E_{NL}(t, \tau, \phi) E_{Pr}^*(t, \tau) dt}{\int E_{Pr}(t, \tau) E_{Pr}^*(t, \tau) dt}, \quad (1)$$

which is valid in the limit of small transmission changes [34]. In Fig. 3(a),  $\Delta T/T_0(\tau, \phi = 0)$  is plotted as a function of  $\tau$ . It contains a positive peak, i.e., a transmission

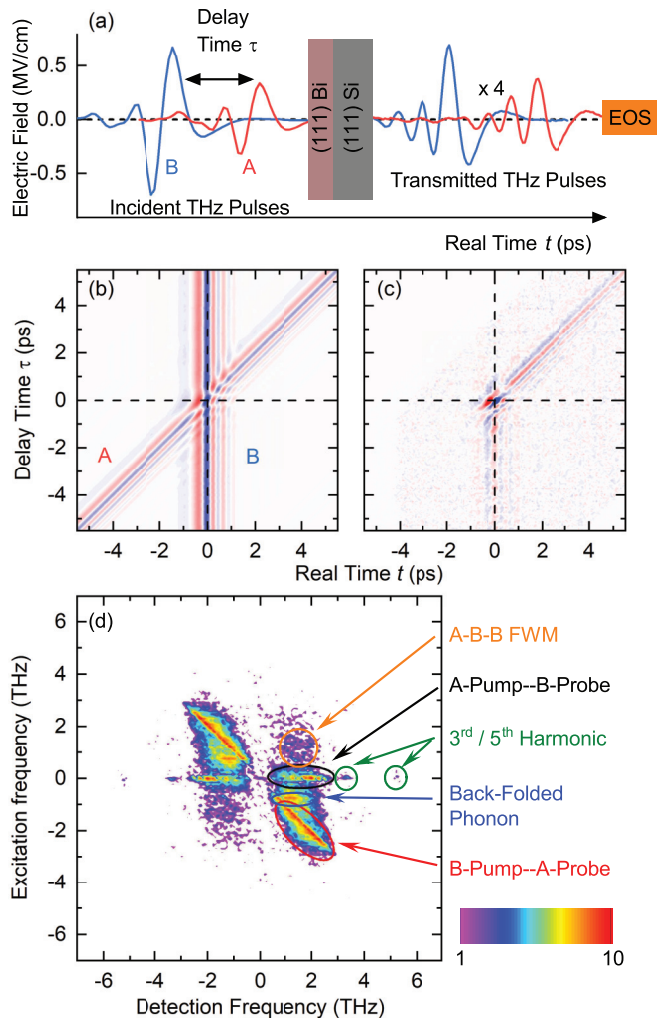


FIG. 2. 2D-THz spectroscopy on Bi. (a) Schematic of the experimental configuration with the incident and transmitted THz pulses A and B detected by electro-optic sampling (EOS). (b) Contour plot of THz electric fields  $E_{AB}(t, \tau)$  of both pulses A and B transmitted through the Bi film as a function of delay time  $\tau$  and real time  $t$  (amplitude scale  $\pm 250$  kV/cm, azimuthal angle  $\phi = 0$ ). (c) Total nonlinear electric field  $E_{NL}(t, \tau)$  emitted from the sample (amplitude scale  $\pm 20$  kV/cm). (d) 2D-Fourier transform  $|E_{NL}(\nu_r, \nu_t)|$  of  $E_{NL}(t, \tau)$  plotted on a logarithmic scale as a function of detection and excitation frequency  $\nu_r$  and  $\nu_t$ , showing different contributions indicated by circles and ovals, respectively.

increase around  $\tau = 0$ , in line with the limited phase shift between  $E_{NL}(t, \tau, \phi)$  and  $E_{Pr}(t, \tau) = E_A(t, \tau)$  when plotted as a function of  $t$  [Fig. 3(c)]. The positive peak has a width of 115 fs. The Fourier transform (inset) of a fit with a Gaussian function (red dashed line) reveals frequency components of up to 6 THz, well above the frequencies contained in the incident THz pulses. This indicates the induced transparency to originate from multiphoton mixing processes. At delay times  $\tau > 0.3$  ps,  $\Delta T/T_0(\tau, \phi = 0)$  has a negative sign and eventually decays on a few-picosecond timescale. The signal is assigned to induced absorption originating from irreversible carrier generation. Correspondingly, at  $\tau = 2$  ps, the electric fields  $E_{NL}(t, \tau = 2, \phi)$  and  $E_{Pr}(t, \tau) = E_A(t, \tau)$  display

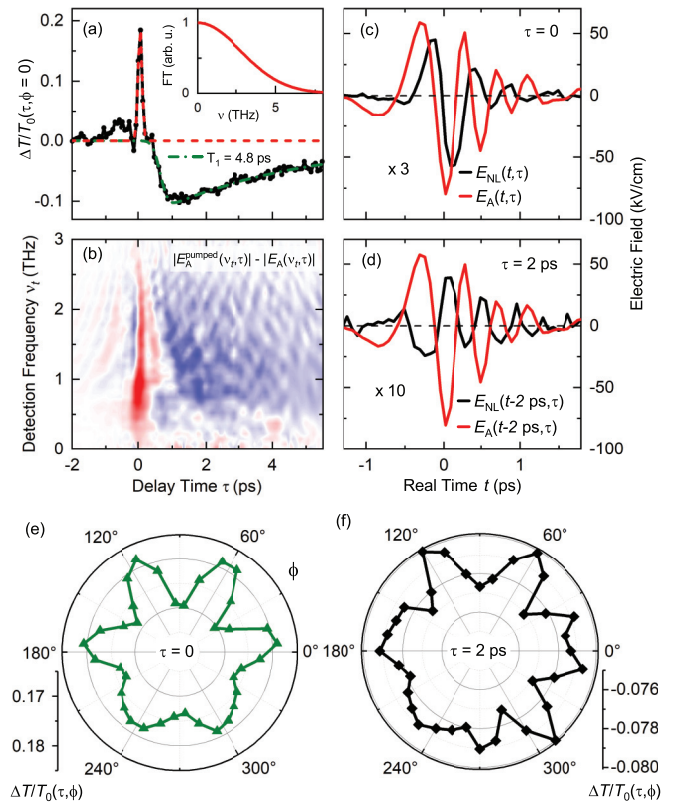


FIG. 3. Pump-induced transmission changes depending on delay time  $\tau$  and azimuthal angle  $\phi$ . (a) Change of transmission  $\Delta T/T_0(\tau, \phi = 0)$ . The green dash-dotted line indicates a fit with a single exponential decay for  $\tau > 0.3$  ps. The red dashed line represents a fit with a Gaussian function of the coherence peak at  $\tau = 0$  and its Fourier transform (inset). (b) Difference spectrum of the amplitude spectra  $|E_A^{\text{pumped}}(\nu_r, \tau)| = |E_{AB}(\nu_r, \tau) - E_B(\nu_r, \tau)|$  and  $|E_A(\nu_r, \tau)|$ . (c, d) Cuts of  $E_{NL}(t, \tau)$  (black line) and  $E_A(t, \tau)$  (red line) at  $\tau = 0$  and  $\tau = 2$  ps. (e, f) Angular dependence of the change of transmission  $\Delta T/T_0(\tau, \phi)$  for delay times  $\tau = 0$  and 2 ps.

opposite phases [Fig. 3(d)]. In the range of sequential interaction with the pump and the probe pulse ( $\tau > 1$  ps), the signal follows a single exponential decay (green dash-dotted line) with a population decay time  $T_1 = 4.8$  ps.

In Fig. 3(b), the differential spectrum  $|E_A^{\text{pumped}}(\nu_r, \tau)| - |E_A(\nu_r, \tau)|$ , with  $|E_A^{\text{pumped}}(\nu_r, \tau)| = |E_{AB}(\nu_r, \tau) - E_B(\nu_r, \tau)|$ , derived by Fourier transforming  $E_{AB}(t, \tau)$ ,  $E_A(t, \tau)$  and  $E_B(t)$  along real time  $t$ , shows the spectrally resolved transmission changes. Similarly to  $\Delta T/T_0(\tau, \phi = 0)$ , it contains a region of enhanced transparency around zero delay and induced absorption for delay times  $\tau > 0.3$  ps. Both effects prevail over the whole (detected) spectral range up to  $\nu_r = 3$  THz.

Figures 3(e) and 3(f) show the change of transmission  $\Delta T/T_0(\tau, \phi)$  for varying azimuthal angles  $\phi$  of the electric field at fixed time delays  $\tau = 0$  and 2 ps. For both delay times, a pronounced angular dependence with sixfold symmetry is observed. At  $\tau = 0$  the positive pump-probe signal is modulated by up to 11%. The negative signal at  $\tau = 2$  ps displays a weaker modulation by about 6%.

Figure 4 shows the nonlinear signals arising from third- and fifth-harmonic generation. The higher harmonic signals

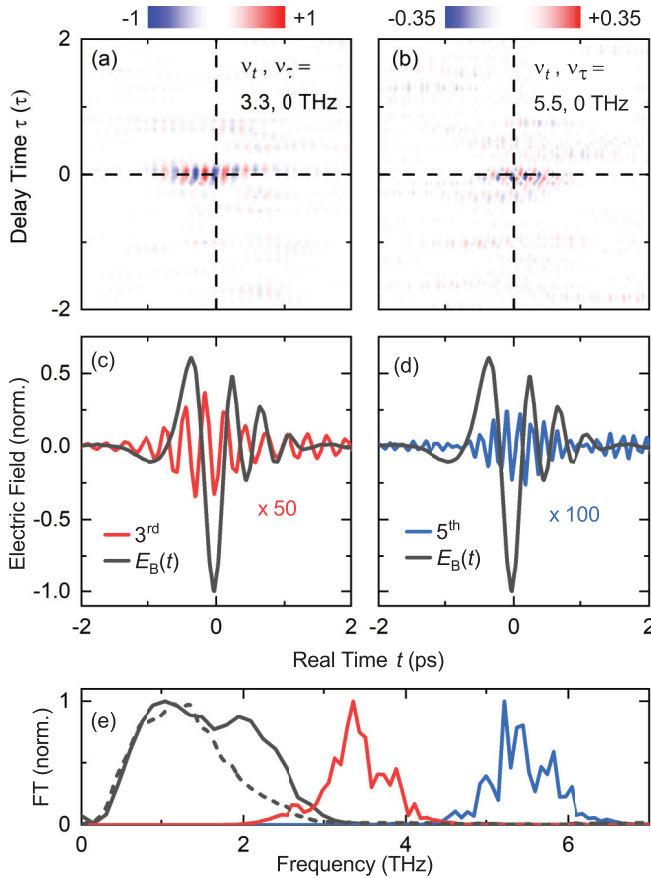


FIG. 4. High-harmonic generation in Bi. (a, b) Fourier back-transforms of third- and fifth-harmonic signals as indicated by green circles in Fig. 2(c) (amplitude scales  $\pm 1$  kV/cm and  $\pm 0.35$  kV/cm). (c, d) Cuts of electric fields in panels (a, b) at  $\tau = 0$  compared to the transmitted THz electric field  $E_B(t)$ . (e) Spectra of the transmitted (solid black line) and the incident THz electric field (dashed black line), and the third- and fifth-harmonic signals in panels (c) and (d) (red and blue lines).

in the time domain plotted in Figs. 4(a) and 4(b) are derived by Fourier back transforms of the regions indicated by the green circles in Fig. 2(d). We would like to remark that the fifth-harmonic signal is very weak and close to the noise limit of our measurement. Both signals occur in a narrow temporal region around  $\tau = 0$ . In Figs. 4(c) and 4(d), cuts at  $\tau = 0$  along real time  $t$  are plotted together with  $E_B(t)$ . In Fig. 4(e) the spectra of the incident and transmitted THz pulses, and the third- and fifth-harmonic signal are shown. The third- and fifth-harmonic signals occur at three and five times the 1.1-THz frequency of the incident THz pulse. The third-harmonic signal spectrally integrated along  $\nu_t$  and  $\nu_\tau$  is a factor of 7 higher than the spectrally integrated noise of the experiment, while the integrated fifth-harmonic signal exceeds the noise by a factor of 4.

In Fig. 5 we analyze the signal arising from coherent phonon oscillations in the sample. In frequency space this phonon signal at a spectral position of  $(\nu_t, \nu_\tau) = (1.2, -0.8)$  THz [blue oval in Fig. 2(d)] spectrally overlaps with the B-pump-A-probe signal. Separating these nonlinear signal contributions from each other by

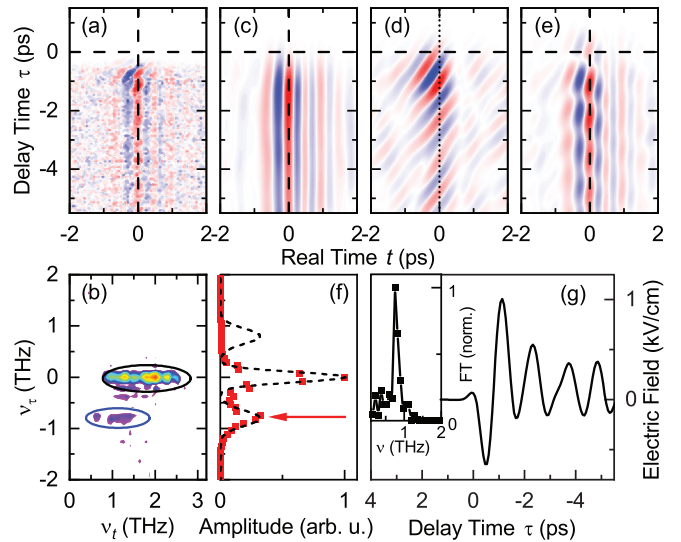


FIG. 5. Coherent phonon oscillations upon THz excitation in Bi. (a)  $E_{NL}(t, \tau)$  for delay times  $\tau < -0.3$  ps (amplitude scale  $\pm 5$  kV/cm). (b) Amplitude of the 2D Fourier transform of the electric field in panel (a) as a function of detection and excitation frequencies  $\nu_t$  and  $\nu_\tau$ . (c, d) Fourier back transforms of the regions indicated by the black and blue ovals, respectively (amplitude scales  $\pm 2$  kV/cm and  $\pm 1$  kV/cm). (e) Sum of filtered signals in panels (c) and (d) (amplitude scale  $\pm 2.5$  kV/cm). (f) Projection of the 2D amplitude spectrum in panel (b) on  $\nu_\tau$ . (g) Oscillatory signal derived by cutting at  $t = 0$  along  $\tau$  through the signal in panel (d) and the corresponding Fourier transform (inset).

Fourier filtering (as done for the higher harmonics signals) is difficult. Instead, we separate the nonlinear signal at negative delay times by setting any contributions  $\tau > -0.3$  ps to zero [Fig. 5(a)]. The 2D Fourier transform of this temporally filtered signal [Fig. 5(b)] reveals a strong A-pump-B-probe signal (black oval) and a second signal at  $(\nu_t, \nu_\tau) = (1.2, -0.8)$  THz (blue oval), well separated from each other in frequency space. A Fourier back transform of the pump-probe signal [Fig. 5(c)] does not contain any oscillatory amplitude variations along  $\tau$ . However, the back transform of the signal indicated by the blue oval [Fig. 5(d)] shows strong oscillations along  $\tau$ , reaching 50% of the pump-probe signal strength. In Fig. 5(e), the sum of these two filtered signals is plotted. The positions of amplitude maxima and minima along the delay time  $\tau$  depend on the particular value of real time  $t$ . Such behavior points to dispersive rather than absorptive modification of the A-pump-B-probe signal.

In Fig. 5(f) the signal in frequency space [indicated by the ovals in Fig. 5(b)] is integrated over the detection frequency  $\nu_t$  and plotted as a function of  $\nu_\tau$ . It shows distinct peaks at  $\nu_\tau = 0$  and  $\nu_\tau = -0.8$  THz. A purely absorptive effect would manifest in spectral sidebands at  $\pm 0.8$  THz, i.e., a symmetric spectrum around  $\nu_\tau = 0$  as indicated schematically by the dashed black line. The observed asymmetry of the spectrum again points to dispersive modifications of the A-pump-B-probe signal, suggesting modifications to both real and imaginary part of the dielectric function of Bi. In Fig. 5(g) a cut along  $\tau$  at  $t = 0$  of the pure oscillatory signal in Fig. 5(d) shows coherent oscillations which arise from

coherent phonon oscillations, as will be discussed below. A Fourier transform (inset) gives an oscillation frequency of 0.8 THz with a spectral width of 0.3 THz (FWHM).

#### IV. DISCUSSION

In this section we discuss (i) the distinction between the perturbative and nonperturbative regime of light-matter interaction, (ii) mechanisms of irreversible electron-hole pair generation, as well as intra- and interband dynamics, and (iii) the excitation-induced symmetry reduction and consequences for the phonon dispersion in the excited Bi crystal.

##### A. Perturbative vs nonperturbative regime

For nonlinear light-matter interaction dominated by a third-order optical susceptibility  $\chi^{(3)}$ , the occurring processes can be described correctly by means of the perturbative expansion in the electric field. As soon as higher-order susceptibilities, e.g.,  $\chi^{(5)}$  and beyond, become relevant simultaneously, the perturbative expansion fails. In this regime of nonperturbative light-matter interaction, it is not possible to assign specific nonlinear signals, e.g., certain spots in Fig. 2(d), to particular orders in a perturbative expansion. For example, a third-harmonic signal [cf. Figs. 4(a) and 4(c)] can be realized by an arbitrary odd number of photons with frequency  $\nu_0$ , whose frequency vectors [35] sum up to  $(\nu_l, \nu_r) = (3\nu_0, 0)$ . In the perturbative regime, however, third-harmonic generation is restricted to the interaction of exactly three photons.

The respective interaction regime is determined by the strength of light-matter coupling, which in the dipole approximation is proportional to the product of the external (THz) electric field with the dipole moments  $d_{\text{VB}\leftrightarrow\text{CB}}(\mathbf{k})$  of electronic interband transitions at certain points in the band structure. The interband transition dipole close to the  $L$  point can be estimated from the interband transition frequency  $\nu_g(\mathbf{k})$  and the Fermi velocity  $v_F$ , given by the gradient of the conduction band, as

$$d_{\text{VB}\leftrightarrow\text{CB}}(\mathbf{k}) = \frac{e p_{\text{VB}\leftrightarrow\text{CB}}(\mathbf{k})}{m 2\pi \nu_g(\mathbf{k})} \approx \frac{e v_F}{2\pi \nu_g(\mathbf{k})}, \quad (2)$$

where  $e$  is the elementary charge,  $m$  the electronic mass, and  $p_{\text{VB}\leftrightarrow\text{CB}}(\mathbf{k})$  the momentum [36]. In the vicinity of regions in  $k$  space with narrow gaps, where  $\nu_g(\mathbf{k})$  is very small and  $v_F$  very large,  $d_{\text{VB}\leftrightarrow\text{CB}}(\mathbf{k})$  diverges. At the  $L$  points in Bi with  $\nu_g = 3.62$  THz and  $v_F \approx 7.6 \times 10^5$  m/s, transition dipole moments reach large values of the order of  $e \times 35$  nm. Details of the band structure directly at  $L$  are given in Appendix A.

The frequency of the incident light field determines positions in  $k$  space at which interband transitions may occur. Our THz driving pulses with center frequencies of 1.1 THz are in resonance with three-photon absorption at the  $L$  point. The excursion of conduction-band electrons in  $k$  space is determined by the vector potential  $A(t) = \int_{-\infty}^t E(t') dt'$ , given by the time integral of the external THz electric field  $E(t)$ . The perturbative expansion is a good approximation if  $\gamma = eA(t)v_F/[\hbar 2\pi \nu_g(\mathbf{k})] \ll 1$ , i.e., if the ponderomotive energy is much smaller than the energy gap, and electrons undergo only small excursions in  $k$  space. For THz excitation

at the  $L$  point, this condition is only fulfilled for field strengths  $< 1$  kV/cm. Light-matter interaction needs to be described in the nonperturbative regime if

$$\gamma = \frac{eA(t)v_F}{\hbar 2\pi \nu_g(\mathbf{k})} = \frac{d_{\text{VB}\leftrightarrow\text{CB}}(\mathbf{k})A(t)}{\hbar} \geq 1, \quad (3)$$

i.e., if the ponderomotive energy exceeds the energy gap, and light-matter interaction dominates the motion of conduction-band electrons. For the THz electric field strengths of some 150 kV/cm applied in our experiments leading to a value of  $\gamma \approx 70$ , light-matter interaction is in the nonperturbative regime.

##### B. Irreversible electron-hole pair generation

The excursion of conduction-band electrons in  $k$  space is given by  $\Delta k(t) = A(t)e/\hbar$ , where  $A(t)$  is the vector potential of a linearly polarized electric field. For our experimental THz field with amplitudes of about 150 kV/cm and frequencies of 1.1 THz, the excursion in  $k$  space has an amplitude of  $\Delta k = 2 \text{ nm}^{-1}$ . Each carrier undergoes such intraband motions, while additional interband transitions occur in the vicinity of the  $L$  points of the band structure, e.g., by field-induced tunneling ionization [37] and interband Rabi flopping [16].

Figures 6(a)–6(c) show schematic electron distributions around an  $L$  point for different strengths of the vector potential  $A(t)$ . In equilibrium, with the vector potential  $A(t) = 0$ , the valence band around the  $L$  point is fully occupied and the conduction band is populated up to the Fermi energy  $E_F$  [Fig. 6(a)]. As the vector potential increases up to  $A(t) = E_F/(ev_F)$ , intraband transitions of conduction-band electrons occur [Fig. 6(b)]. For larger values of  $A(t)$ , electrons driven to the  $L$  points experience diverging interband transition dipole moments [cf. Eq. (2)] and undergo interband transitions, as illustrated in Fig. 6(c). All electrons within a range defined by the amplitude of the excursion  $\Delta k$  are moved through the  $L$  point, where the dipole moment diverges and electrons are efficiently excited into the conduction band. As shown by Ishikawa [12], the simultaneous variation of the interband frequency  $\nu_g[\mathbf{k}(t)]$  and the transition dipole moment  $d_{\text{VB}\leftrightarrow\text{CB}}[\mathbf{k}(t)]$  leads predominantly to interband transitions of electrons within this range. Electrons outside of this range, not passing along  $L$ , however, predominantly undergo intraband motions. In absence of scattering events, electron-hole pairs recombine coherently, corresponding to a fully reversible excitation. In the presence of electron-electron and electron-phonon scattering, the quantum phase of the excitations is destroyed on a femtosecond timescale, resulting in the generation of an electron-hole plasma.

Figure 6(d) shows the (calculated) electronic conduction-band structure around an  $L$  point as a function of  $k_{LW}$  ( $W - L - W$  direction) and  $k_{LU}$  ( $L - U - L$  direction) [27]. The  $k$  range of electrons being excited into the conduction band is indicated by a magenta rectangle. In the direct vicinity of the  $L$  point, the band structure shows a circular symmetry. Moving further away from  $L$ , the band structure reflects the hexagonal crystal structure of Bi. The deviations get most obvious when comparing cuts along the orthogonal  $k$  directions  $k_{LU}$ ,  $k_{LW}$ , and  $k_{L\Gamma}$  ( $\Gamma - L - \Gamma$  direction) of the valence and conduction bands [Fig. 6(e)]. In the direct vicinity of  $L$ , the bands coin-

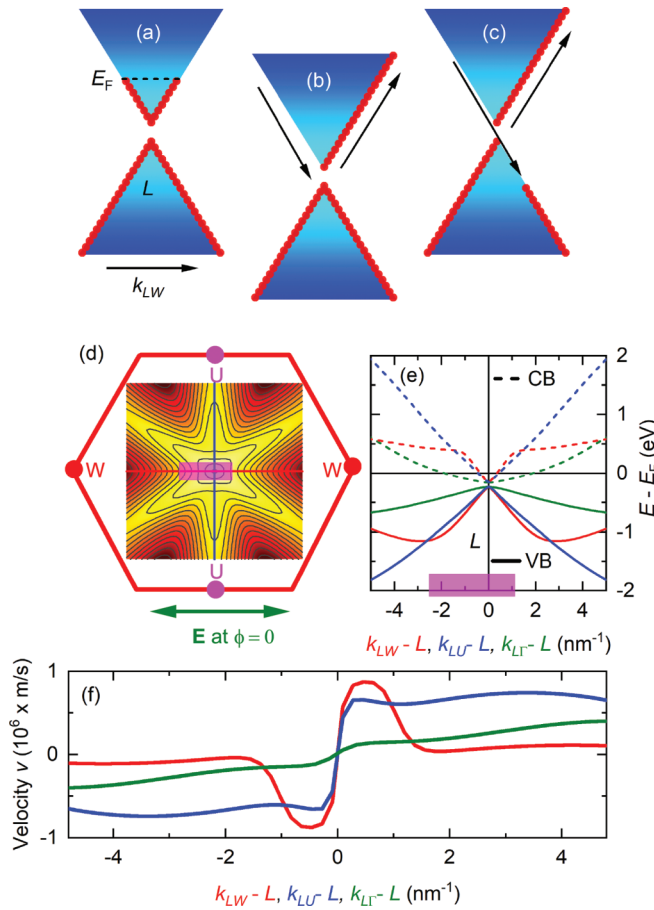


FIG. 6. Band structure, and intra- and interband dynamics in the vicinity of the  $L$  point in Bi. (a)–(c) Schematic of electron (red circles) and hole distributions in the conelike band structure around the  $L$  point for different vector potentials. (a)  $A = 0$ : conduction band is filled up to the Fermi energy  $E_F$ . (b)  $A = E_F/(ev_F)$ : the vector potential accounts for intraband motions of conduction-band electrons in a specific  $k$  direction. (c)  $A > E_F/(ev_F)$ : both intraband and interband transitions take place, accounting for (coherently reversible) electron-hole pair generation. (d) 2D conduction-band structure around an  $L$  point in the  $k_{LU}$  ( $U-L-U$ ) direction and in the  $k_{LW}$  ( $W-L-W$ ) direction on one of the hexagonal side facets [cf. Fig. 1(c)], calculated with DFT code FLEUR [27,28]. Electrons in the region indicated by the magenta rectangle undergo interband transitions for an electric field in  $W-L-W$  direction as indicated by the green double arrow. The length of this rectangle along  $k_{LW}$  is determined by the amplitude of the electron excursion in  $k$  space for an applied electric field of 150 kV/cm. (e) Cuts through the valence and conduction-band structures (VB and CB: solid and dashed lines, respectively) along the orthogonal  $k$  directions  $k_{LU}$  (blue lines),  $k_{LW}$  (red lines), and  $k_{L\Gamma}$  ( $\Gamma-L-\Gamma$ , green lines). (f) Electron velocity in orthogonal  $k$  directions in the three-dimensional conduction-band structure.

side, whereas for increasing distance from  $L$ , deviations from a perfect cone occur. At distances above  $\Delta k = 1.5 \text{ nm}^{-1}$ , such deviations become most pronounced. Here, the band structure in orthogonal  $k$  directions has strongly different gradients, and thus the electron velocities, as derived by  $v = \hbar^{-1} \nabla_{\vec{k}} E(\vec{k})$  and plotted in Fig. 6(f), are highly  $k$  direction dependent.

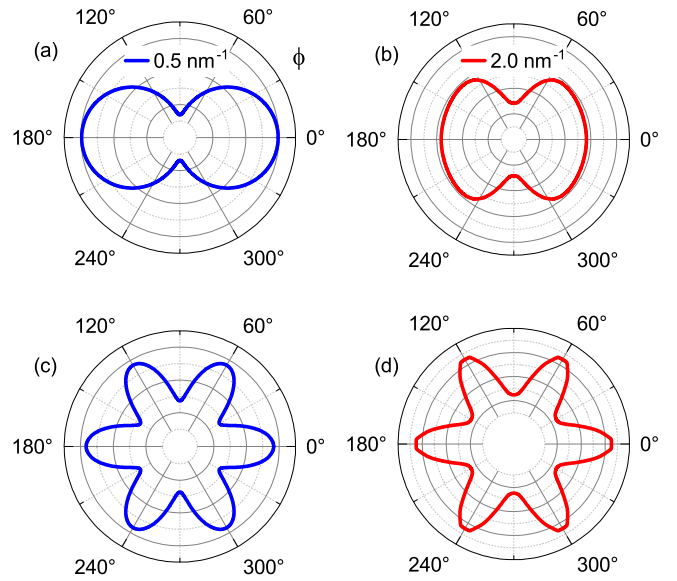


FIG. 7. (a, b) Azimuthal dependence of the energy  $E(\mathbf{k})$  electrons obtain in the vicinity of a single  $L$  point when experiencing excursions in  $k$  space of  $\Delta k = 0.5$  and  $2 \text{ nm}^{-1}$ , respectively. Such excursions are due to an external electric field in a plane perpendicular to the  $(111)$  crystal axis. The angle  $\phi$  is the azimuthal angle around the  $(\Gamma, T)$  axis of the Brillouin zone. The radial scales are from 0 to 0.35 eV in (a), and from 0 to 0.9 eV in (b). (c, d) Band energy  $E(\mathbf{k})$  summed over all six  $L$  facets for  $k$  space excursions of  $0.5$  and  $2 \text{ nm}^{-1}$ . The respective radial scales are from 0.56 to 0.63 eV in (c) and from 1.3 to 1.7 eV in (d).

We now address the anisotropy of an optical excitation induced by a linearly polarized THz electric field [Figs. 3(e) and 3(f)]. Any linearly polarized field has a different orientation regarding the different  $L$  points [38], as illustrated in Fig. 1(b). If electrons at two oppositely positioned  $L$  points are excited in the  $W-L-W$  direction, lying in the plane perpendicular to the  $[111]$  direction in real space, electrons at the other four  $L$  points are driven into different directions concerning the respective  $L$  point. These different directions can be expressed as a superposition of orthogonal directions  $k_{LW}$ ,  $k_{LU}$ , and  $k_{L\Gamma}$ . In particular, the projection of the electric field  $\mathbf{E}_{\text{THz}}$  on the  $k$  direction can be expressed as

$$\begin{aligned} \mathbf{E}_{\text{THz}} &= \mathbf{E}_{LW} + \mathbf{E}_{LU} + \mathbf{E}_{L\Gamma} \\ &= E_{\text{THz}} [\hat{\mathbf{k}}_{LW} \sin(\phi) + \hat{\mathbf{k}}_{LU} \cos(\phi) \sin(\beta) \\ &\quad + \hat{\mathbf{k}}_{L\Gamma} \cos(\phi) \cos(\beta)], \end{aligned} \quad (4)$$

with the azimuthal angle  $\phi$  around the  $(\Gamma, T)$  axis of the Brillouin zone [cf. Fig. 1(c)], the tilting angle  $\beta = 18.2^\circ$  between the  $L-U$  and  $T-\Gamma$  direction, and the unit vectors  $\hat{\mathbf{k}}_i$ .

A calculation of the energy  $E(\mathbf{k})$  of electrons at fixed electron excursions  $\Delta k = 0.5 \text{ nm}^{-1}$  and  $2 \text{ nm}^{-1}$  in two of the conduction band  $L$  valleys gives the azimuthal dependencies shown in Figs. 7(a) and 7(b). The dumbbell shape reflects deviations of the band structure along different  $k$  directions and allows for distinguishing a preferred direction. For small electron excursions [Fig. 6(f)], the preferred direction is parallel to  $k_{LW}$ , having the largest Fermi velocity [cf. Fig. 7(a)]. For

electron excursions exceeding  $1.5 \text{ nm}^{-1}$ , the band structure in  $k_{LW}$  direction flattens and  $v_F$  decreases by about 90%. In consequence, the contribution of the band structure in  $k_{L\Gamma}$  and  $k_{LU}$  direction to the maximum energy conduction-band electrons carry increases. As a result, the dumbbell shape in Fig. 7(b) is somewhat compressed compared with the case of small electron excursions in Fig. 7(a). The superposition of such dependencies for all six  $L$  valleys are presented in Figs. 7(c) and 7(d). Here, one observes an essentially round, i.e., isotropic distribution, superimposed by a sixfold angular modulation, i.e., anisotropy, of limited amplitude on top. The observed sixfold symmetry only occurs in the nonperturbative regime, i.e., is absent in the linear regime. It can also be understood from a simple picture of a tight-binding model as discussed in Appendix B.

The anisotropy of the band structure with respect to a linearly polarized THz field leads to an anisotropic optical excitation of the material, both in the perturbative and nonperturbative regime of light-matter interaction. This anisotropy in carrier generation is counteracted by inter- $L$ -valley scattering of electrons on a typically sub-100-fs timescale, a process which tends to generate equal electron populations in the six  $L$  valleys. For holes, the scattering scenario is more complex and includes a predominant scattering to the two  $T$  valleys, with their maxima at a lower hole energy. Eventually, electron-hole recombination with a time constant on the order of 5 ps (cf. Fig. 3(a), [25]) reestablishes the equilibrium carrier distribution.

The angle-resolved pump-probe signals in Figs. 3(e) and 3(f) display a sixfold symmetry, which agrees qualitatively with the calculations shown in Fig. 7. While the pump-probe signal at delay  $\tau = 0$  [Fig. 3(e)] is due to a superposition of different nonlinear interaction pathways and, thus, is difficult to interpret, the signal at  $\tau = 2$  ps [Fig. 3(f)] is in the regime of a sequential interaction with the pump and the probe pulse. Although typical intervalley scattering times of electrons are very short compared to the picosecond THz pulse duration, one observes a residual anisotropy of the pump-probe signal. This persistence of symmetry breaking is assigned to the significant anisotropic carrier generation rate in the tail of the pump pulse, which allows for keeping up a residual symmetry breaking. In summary, the transient carrier distribution existing during and immediately after the THz pump pulse consists of holes, predominantly in the  $T$  valleys, and electrons in unequally populated  $L$  valleys. It should be noted that this mechanism of symmetry breaking is absent in quasi-two-dimensional graphene, a major difference between the isotropic two-dimensional and the anisotropic three-dimensional conelike band structures of graphene and Bi. The breaking of the Bi equilibrium symmetry opens up new pathways of optical phonon excitation, as will be discussed next.

### C. Symmetry breaking and displacive excitation of back-folded phonons

The transient charge distribution described in the previous section extends over two neighboring elementary cells, with a periodicity in  $\mathbf{k}_X$  direction. The  $k$  vector at a certain  $X$  point is identical to the difference of the  $k$  vectors at the  $T$  point and a

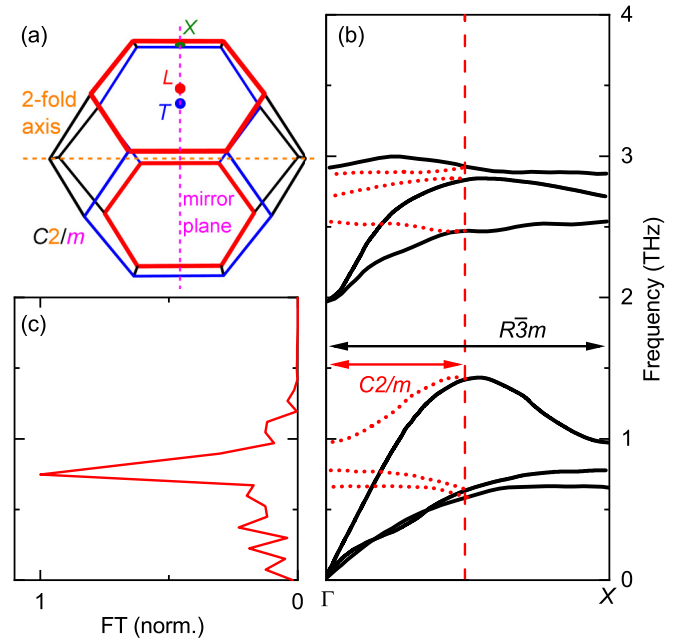


FIG. 8. (a) Brillouin zone of Bi in the rhombohedral space group  $R\bar{3}m$ , rotated in a way so that the (lower) symmetry of the  $X$  points with its twofold rotational axis (dashed orange line) and a single mirror plane (dashed magenta line) becomes apparent. (b) Calculated phonon dispersion in the Brillouin zone (BZ) of the rhombohedral space group  $R\bar{3}m$  (Fig. 3 in [39]). In the monoclinic space group  $C2/m$ , phonons at  $X$  are back-folded to  $\Gamma$ . (c) Fourier transform of phonon oscillations observed in the A-pump-B-probe signal [cf. inset in Fig. 5(g)].

certain  $L$  point  $\mathbf{k}_T$  and  $\mathbf{k}_L$ , i.e.,  $\mathbf{k}_X = \mathbf{k}_T - \mathbf{k}_L$ . This symmetry is identical to the symmetry properties of the  $X$  points in the unexcited Bi sample with a twofold rotational axis and a single mirror plane [cf. Fig. 8(a)]. More precisely, nonperturbative excitation of Bi reduces the total crystal symmetry from the rhombohedral space group  $R\bar{3}m$  with two atoms per elementary cell to the monoclinic space group  $C2/m$  (of the  $X$  points) with four atoms per elementary cell.

In Fig. 8(b), the calculated phonon dispersion in  $k$  space spanning from  $\Gamma$  to  $X$  is shown for the rhombohedral space group  $R\bar{3}m$  (black solid lines) with two atoms per elementary cell [39]. The symmetry reduction upon nonequilibrium carrier generation results in a backfolding of acoustic and optical phonon branches from the  $X$  to the  $\Gamma$  point [dotted lines in Fig. 8(b)]. In particular, backfolding of the acoustic branches leads to three additional optical phonons at  $\Gamma$  with frequencies of 0.66, 0.76, and 0.98 THz.

All phonons at the  $\Gamma$  point are accessible via displacive excitation, i.e., carrier generation induces a shift of the vibrational potential minimum along the phonon coordinate and thus a displacement or elongation of the phonon. A coherent superposition of several phonon states results in coherent phonon wave-packet motions, which, through electron-phonon coupling, manifest in a periodic change of the THz dielectric function. The oscillatory component of the A-pump-B-probe signal in Fig. 5 is due to phonon wave-packet motions with a frequency of 0.8 THz. In Fig. 8(c) the Fourier transform of this signal [cf. inset in Fig. 5(g)] is put in

relation to the back-folded phonon dispersion in Fig. 8(b). The spectrum can clearly be assigned to back-folded phonons at  $\Gamma$  in the monoclinic space group. The linewidth of the spectrum does not allow for distinguishing which phonon is observed and may arise from a superposition of all three phonons. It should be noted that back-folded optical phonons in Bi have been observed in very recent femtosecond x-ray diffraction experiments with excitation pulses around 60 THz [40].

Displacively excited phonons back-folded from  $X$  to  $\Gamma$  possess the (reduced) symmetry of the monoclinic space group  $C2/m$ . Thus the reduced crystal symmetry is preserved for the phonon lifetime, even though the anisotropic carrier distribution becomes isotropic on the much faster timescale of inter- $L$ -valley scattering.

## V. CONCLUSIONS

In conclusion, 2D-THz spectroscopy in the nonperturbative regime of light-matter interaction reveals nonequilibrium carrier generation via quantum pathways around the  $L$  points of the band structure of bismuth. Efficient interband excitation is facilitated by the very large THz interband transition dipole at the  $L$  points. Pump pulses around 1.1 THz, which are linearly polarized in a plane perpendicular to the [111] direction in real space, induce a transient reduction of crystal symmetry by the preferential population of two out of six  $L$  valleys and a subsequent scattering of photoexcited holes to the  $T$  points. This behavior manifests in a dependence of THz pump-probe signals on the azimuthal crystal orientation. The transient symmetry reduction leads to a backfolding of phonon branches from the  $X$  to the  $\Gamma$  points, which allows for displacive excitation of back-folded phonons. The experiments demonstrate coherent wave-packet motions of back-folded phonons at frequencies around 0.8 THz. On top of such findings, the nonperturbative character of light-matter interaction gives rise to high-harmonic generation, in particular, the third and fifth harmonic of the THz fundamental frequency.

In general, our results are applicable to other narrow-gap materials, allowing to directly modify symmetry properties and coherently excite phonons that cannot be accessed via displacive excitation in equilibrium symmetry.

## ACKNOWLEDGMENTS

Funding by the Deutsche Forschungsgemeinschaft (DFG, German Research Foundation) via Grant No. WO 558/14-1 to M.W. and through Project B04 of the Collaborative Research Center SFB 1242, “Nonequilibrium Dynamics of Condensed Matter in the Time Domain” (Project No. 278162697), is appreciated.

## APPENDIX A: BAND STRUCTURE AT $L$ POINT

Density functional theory (DFT) calculations considering the local density approximation (LDA) of the exchange-correlation functional typically give accurate results for the valence-band dispersion of band structures. However, the energy gaps and the exact band alignment is not reproduced

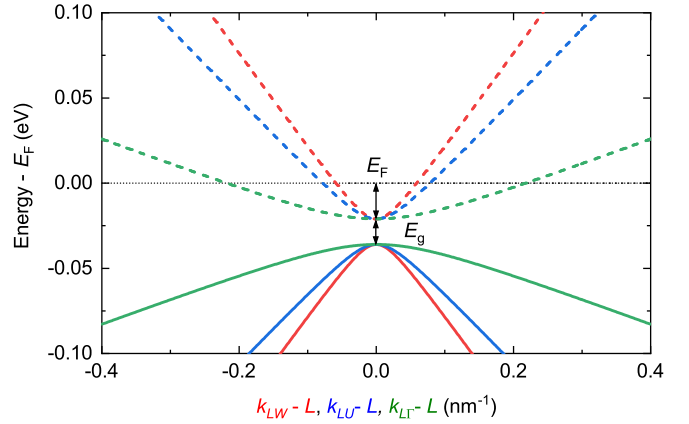


FIG. 9. Band structure in the vicinity of the  $L$  point along orthogonal direction in  $k$  space, calculated by a hyperbolic approximation following Eq. (A1). Solid lines correspond to the valence and dashed lines to the conduction bands.

accurately. In the case of germanium, for instance, LDA delivers an energy gap below zero instead of 0.744 eV [41]. Specifically at the  $L$  point of Bi with its narrow 15-meV energy gap and accordingly large dipole moments on the order of  $e \times 35$  nm [cf. (2)], accurate information about the band structure is necessary. It has been shown for Bi that calculations within a quasiparticle self-consistent GW method (QSGW) cure inadequacies present within LDA and are in excellent agreement with experimental results (cf. Fig. 2(b) and Table I of Ref. [27]). Further, we would like to remark that the three-dimensional band structure in the vicinity of the  $L$  point can be estimated using a simple hyperbolic approximation, i.e.,

$$E_{CB/VB}(\mathbf{k}) = -E_F - E_g^L/2 \pm \left[ (E_g^L/2)^2 + (\hbar v_F^{LW} k_{LW})^2 + (\hbar v_F^{LU} k_{LU})^2 + (\hbar v_F^{L\Gamma} k_{L\Gamma})^2 \right]^{1/2}, \quad (\text{A1})$$

where  $v_F^{LW} = 0.89 \times 10^6$  m/s,  $v_F^{LU} = 0.67 \times 10^6$  m/s, and  $v_F^{L\Gamma} = 0.24 \times 10^6$  m/s are constant Fermi velocities in orthogonal band directions, and  $E_g^L = 15$  meV is the energy gap and  $E_F = 21$  meV the Fermi energy at  $L$ . The result of such calculations is presented in Fig. 9.

## APPENDIX B: SYMMETRY ASPECTS IN THE PERTURBATIVE REGIME OF LIGHT-MATTER INTERACTION

In the perturbative expansion, different nonlinear orders are expressed in terms of susceptibility tensors, i.e.,  $\chi_{ij}^{(1)}$  for the linear response,  $\chi_{ijkl}^{(3)}$  for the third-order response,  $\chi_{ijklmn}^{(5)}$  for the fifth-order response, etc. The dependency of such nonlinearities on the crystal orientation is dictated by the selection rules according to the crystal symmetry of Bi. Linearly polarized incident electric fields lying in the basal ( $xy$ ) plane of Bi account together with parallel nonlinear currents for circular symmetry in the case of the first- and third-order response, i.e.,  $\chi_{xx}^{(1)} = \chi_{yy}^{(1)}$  and  $\chi_{xxxx}^{(3)} = \chi_{yyyy}^{(3)}$ . However, for the fifth-order nonlinearity, the symmetry becomes hexagonal, i.e.,  $\chi_{xxxxxx}^{(5)} \neq \chi_{yyyyyy}^{(5)}$  [42,43].

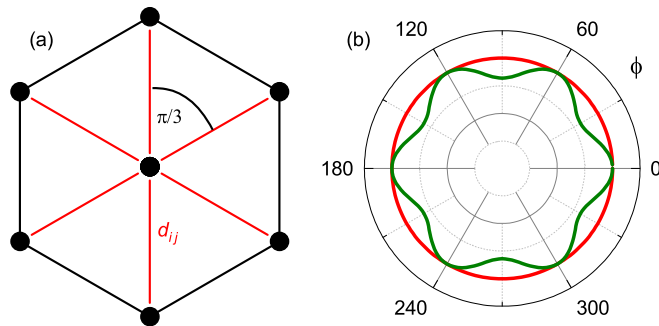


FIG. 10. Symmetry aspects within the perturbative expansion. (a) Top view of the crystal structure of Bi. The black circles indicate atomic positions. In the tight-binding model all electronic charge is located at the atoms. The black and red lines indicate interatomic bonds with dipole moments  $d_{ij}$ . (b) Azimuthal dependence of  $\chi^{(3)}$  (red line) and  $\chi^{(5)}$  (green line), calculated in a simple picture assuming the tight-binding model.

This can be illustrated in a simple picture of a tight-binding model in which all charges are located at the Bi atoms in a plane with hexagonal crystal structure, and transition dipole moments only exist along the bonds between these atoms,

i.e., the angle between transition dipole moments is  $\pi/3$ , as illustrated in Fig. 10(a). In the perturbative expansion, the strength of the  $n$ th perturbative order  $\chi^{(n)}$  is proportional to the  $(n+1)$ -th power of the transition dipole moment. Summing over all six transition dipole moments for a given field direction determined by the azimuthal angle  $\phi$  gives the angular dependence in the respective order of the perturbative expansion  $n$ :

$$\begin{aligned} \chi^{(n)} &\propto \sum_{k=0}^5 \cos\left(\phi + \frac{k \cdot \pi}{3}\right)^{n+1} \\ &\rightarrow \chi^{(1)} \propto 3 \\ &\rightarrow \chi^{(3)} \propto \frac{9}{4} \\ &\rightarrow \chi^{(5)} \propto \frac{3}{16} \cos(6\phi) + \frac{15}{8} \\ &\rightarrow \chi^{(7)} \propto \frac{135}{256} \cos(6\phi) + \frac{105}{64}. \end{aligned} \quad (\text{B1})$$

The  $\cos(6\phi)$  dependence in the fifth and seventh order of the perturbative expansion directly corresponds to the sixfold azimuthal angular dependence [green curve in Fig. 10(b)], which vanishes for lower-order nonlinearities.

- 
- [1] A. Leitenstorfer, S. Hunsche, J. Shah, M. C. Nuss, and W. H. Knox, Femtosecond Charge Transport in Polar Semiconductors, *Phys. Rev. Lett.* **82**, 5140 (1999).
- [2] W. Kuehn, P. Gaal, K. Reimann, M. Woerner, T. Elsaesser, and R. Hey, Coherent Ballistic Motion of Electrons in a Periodic Potential, *Phys. Rev. Lett.* **104**, 146602 (2010).
- [3] T. Rybka, M. Ludwig, M. F. Schmalz, V. Knittel, D. Brida, and A. Leitenstorfer, Sub-cycle optical phase control of nanotunneling in the single-electron regime, *Nat. Photonics* **10**, 667 (2016).
- [4] W. Kuehn, P. Gaal, K. Reimann, M. Woerner, T. Elsaesser, and R. Hey, THz-induced interband tunneling of electrons in GaAs, *Phys. Rev. B* **82**, 075204 (2010).
- [5] C. Somma, K. Reimann, C. Flytzanis, T. Elsaesser, and M. Woerner, High-Field Terahertz Bulk Photovoltaic Effect in Lithium Niobate, *Phys. Rev. Lett.* **112**, 146602 (2014).
- [6] S. Ghimire, A. D. DiChiara, E. Sistrunk, P. Agostini, L. F. DiMauro, and D. A. Reis, Observation of high-order harmonic generation in a bulk crystal, *Nat. Phys.* **7**, 138 (2011).
- [7] O. Schubert, M. Hohenleutner, F. Langer, B. Urbanek, C. Lange, U. Huttner, D. Golde, T. Meier, M. Kira, S. W. Koch, and R. Huber, Sub-cycle control of terahertz high-harmonic generation by dynamical Bloch oscillations, *Nat. Photonics* **8**, 119 (2014).
- [8] F. Sekiguchi, G. Yumoto, H. Hirori, and Y. Kanemitsu, Polarization anomaly in high harmonics in the crossover region between perturbative and extreme nonlinearity in GaAs, *Phys. Rev. B* **106**, L241201 (2022).
- [9] G. Wang, A. Chernikov, M. M. Glazov, T. F. Heinz, X. Marie, T. Amand, and B. Urbaszek, Colloquium: Excitons in atomically thin transition metal dichalcogenides, *Rev. Mod. Phys.* **90**, 021001 (2018).
- [10] A. Autere, H. Jussila, Y. Dai, Y. Wang, H. Lipsanen, and Z. Sun, Nonlinear optics with 2D layered materials, *Adv. Mater.* **30**, 1705963 (2018).
- [11] E. J. Sie, C. M. Nyby, C. D. Pemmaraju, S. J. Park, X. Shen, J. Yang, M. C. Hoffmann, B. K. Ofori-Okai, R. Li, A. H. Reid, S. Weathersby, E. Mannebach, N. Finney, D. Rhodes, D. Chenet, A. Antony, L. Balicas, J. Hone, T. P. Devereaux, T. F. Heinz *et al.*, An ultrafast symmetry switch in a Weyl semimetal, *Nature (London)* **565**, 61 (2019).
- [12] K. L. Ishikawa, Nonlinear optical response of graphene in time domain, *Phys. Rev. B* **82**, 201402(R) (2010).
- [13] P. Bowlan, E. Martinez-Moreno, K. Reimann, T. Elsaesser, and M. Woerner, Ultrafast terahertz response of multi-layer graphene in the nonperturbative regime, *Phys. Rev. B* **89**, 041408(R) (2014).
- [14] T. Higuchi, C. Heide, K. Ullmann, H. B. Weber, and P. Hommelhoff, Light-field-driven currents in graphene, *Nature (London)* **550**, 224 (2017).
- [15] H. A. Hafez, S. Kovalev, J.-C. Deinert, Z. Mics, B. Green, N. Awari, M. Chen, S. Germanskiy, U. Lehnert, J. Teichert, Z. Wang, K.-J. Tielrooij, Z. Liu, Z. Chen, A. Narita, K. Müllen, M. Bonn, M. Gensch, and D. Turchinovich, Extremely efficient terahertz high-harmonic generation in graphene by hot Dirac fermions, *Nature (London)* **561**, 507 (2018).
- [16] O. D. Mücke, T. Tritschler, M. Wegener, U. Morgner, and F. X. Kärtner, Signatures of Carrier-Wave Rabi Flopping in GaAs, *Phys. Rev. Lett.* **87**, 057401 (2001).
- [17] K. Sokolowski-Tinten, C. Blome, J. Blums, A. Cavalleri, C. Dietrich, A. Tarasevitch, I. Uschmann, E. Förster, M. Kammler, M. Horn-von Hoegen, and D. von der Linde, Femtosecond x-ray measurement of coherent lattice vibrations near the Lindemann stability limit, *Nature (London)* **422**, 287 (2003).

- [18] D. M. Fritz, D. A. Reis, B. Adams, R. A. Akre, J. Arthur, C. Blome, P. H. Bucksbaum, A. L. Cavalieri, S. Engemann, S. Fahy, R. W. Falcone, P. H. Fuoss, K. J. Gaffney, M. J. George, J. Hajdu, M. P. Hertlein, P. B. Hillyard, M. Horn-von Hoegen, M. Kammler, J. Kaspar *et al.*, Ultrafast bond softening in bismuth: Mapping a solid's interatomic potential with x-rays, *Science* **315**, 633 (2007).
- [19] S. L. Johnson, P. Beaud, C. J. Milne, F. S. Krasniqi, E. S. Zijlstra, M. E. Garcia, M. Kaiser, D. Grolimund, R. Abela, and G. Ingold, Nanoscale Depth-Resolved Coherent Femtosecond Motion in Laser-Excited Bismuth, *Phys. Rev. Lett.* **100**, 155501 (2008).
- [20] S. L. Johnson, P. Beaud, E. Vorobeva, C. J. Milne, É. D. Murray, S. Fahy, and G. Ingold, Directly Observing Squeezed Phonon States with Femtosecond X-Ray Diffraction, *Phys. Rev. Lett.* **102**, 175503 (2009).
- [21] S. L. Johnson, P. Beaud, E. Vorobeva, C. J. Milne, É. D. Murray, S. Fahy, and G. Ingold, Non-equilibrium phonon dynamics studied by grazing-incidence femtosecond x-ray crystallography, *Acta Crystallogr. A* **66**, 157 (2010).
- [22] W. Lu, M. Nicoul, U. Shymanovich, A. Tarsevitch, M. Kammler, M. Horn-von Hoegen, D. von der Linde, and K. Sokolowski-Tinten, Extreme phonon softening in laser-excited bismuth—Towards an inverse Peierls-transition, *MRS Proc. Online Proc. Libr.* **1230**, 305 (2009).
- [23] M. Hase, M. Kitajima, S. I. Nakashima, and K. Mizoguchi, Dynamics of Coherent Anharmonic Phonons in Bismuth Using High Density Photoexcitation, *Phys. Rev. Lett.* **88**, 067401 (2002).
- [24] D. Boschetto, E. G. Gamaly, A. V. Rode, B. Luther-Davies, D. Glijer, T. Garl, O. Albert, A. Rousse, and J. Etchepare, Small Atomic Displacements Recorded in Bismuth by the Optical Reflectivity of Femtosecond Laser-Pulse Excitations, *Phys. Rev. Lett.* **100**, 027404 (2008).
- [25] I. Timrov, T. Kampfrath, J. Faure, N. Vast, C. R. Ast, C. Frischkorn, M. Wolf, P. Gava, and L. Perfetti, Thermalization of photoexcited carriers in bismuth investigated by time-resolved terahertz spectroscopy and ab initio calculations, *Phys. Rev. B* **85**, 155139 (2012).
- [26] P. Cucka and C. S. Barrett, The crystal structure of Bi and of solid solutions of Pb, Sn, Sb and Te in Bi, *Acta Cryst.* **15**, 865 (1962).
- [27] I. Aguilera, C. Friedrich, and S. Blügel, Electronic phase transitions of bismuth under strain from relativistic self-consistent *GW* calculations, *Phys. Rev. B* **91**, 125129 (2015).
- [28] D. Wortmann, G. Michalíček, R. Hilgers, A. Neukirchen, H. Janssen, U. Grytsiuk, J. Broeder, and C.-R. Gerhorst, DFT code FLEUR, <http://www.flapw.de>.
- [29] K. Reimann, M. Woerner, and T. Elsaesser, Two-dimensional terahertz spectroscopy of condensed-phase molecular systems, *J. Chem. Phys.* **154**, 120901 (2021).
- [30] M. Kammler and M. Horn-von Hoegen, Low energy electron diffraction of epitaxial growth of bismuth on Si(111), *Surf. Sci.* **576**, 56 (2005).
- [31] T. Payer, C. Klein, M. Acet, V. Ney, M. Kammler, F.-J. M. zu Heringdorf, and M. Horn-von Hoegen, High-quality epitaxial Bi(111) films on Si(111) by isochronal annealing, *Thin Solid Films* **520**, 6905 (2012).
- [32] A. Ghalgaoui, L.-M. Koll, B. Schütte, B. P. Fingerhut, K. Reimann, M. Woerner, and T. Elsaesser, Field-induced tunneling ionization and terahertz-driven electron dynamics in liquid water, *J. Phys. Chem. Lett.* **11**, 7717 (2020).
- [33] C. Somma, K. Reimann, M. Woerner, T. Kiel, K. Busch, A. Braun, M. Matalla, K. Ickert, and O. Krüger, Mid-infrared beam splitter for ultrashort pulses, *Opt. Lett.* **42**, 2918 (2017).
- [34] T. Elsaesser, K. Reimann, and M. Woerner, *Concepts and Applications of Nonlinear Terahertz Spectroscopy* (Morgan & Claypool Publishers, San Rafael, CA, 2019).
- [35] M. Woerner, W. Kuehn, P. Bowlan, K. Reimann, and T. Elsaesser, Ultrafast two-dimensional terahertz spectroscopy of elementary excitations in solids, *New J. Phys.* **15**, 025039 (2013).
- [36] B. Gu, N. H. Kwong, and R. Binder, Relation between the interband dipole and momentum matrix elements in semiconductors, *Phys. Rev. B* **87**, 125301 (2013).
- [37] I. Katayama, H. Kawakami, T. Hagiwara, Y. Arashida, Y. Minami, L.-W. Nien, O. S. Handegard, T. Nagao, M. Kitajima, and J. Takeda, Terahertz-field-induced carrier generation in  $\text{Bi}_{1-x}\text{Sb}_x$  Dirac electron systems, *Phys. Rev. B* **98**, 214302 (2018).
- [38] P. Zhou, C. Streubühr, M. Ligges, T. Brazda, T. Payer, F. M. zu Heringdorf, M. Horn-von Hoegen, and D. von der Linde, Transient anisotropy in the electron diffraction of femtosecond laser-excited bismuth, *New J. Phys.* **14**, 103031 (2012).
- [39] L. E. Díaz-Sánchez, A. H. Romero, and X. Gonze, Phonon band structure and interatomic force constants for bismuth: Crucial role of spin-orbit interaction, *Phys. Rev. B* **76**, 104302 (2007).
- [40] A. Koç, I. Gonzalez-Vallejo, M. Runge, A. Ghalgaoui, K. Reimann, L. Kremeyer, F. Thiemann, M. Horn-von Hoegen, K. Sokolowski-Tinten, M. Woerner, and T. Elsaesser, Quantum pathways of carrier and coherent phonon excitation in bismuth, *Phys. Rev. B* **107**, L180303 (2023).
- [41] M. S. Hybertsen and S. G. Louie, Electron correlation in semiconductors and insulators: Band gaps and quasiparticle energies, *Phys. Rev. B* **34**, 5390 (1986).
- [42] M. I. Aroyo, J. M. Perez-Mato, C. Capillas, E. Kroumova, S. Ivantchev, G. Madariaga, A. Kirov, and H. Wondratschek, Bilbao Crystallographic Server: I. Databases and crystallographic computing programs, *Z. Kristallogr. Cryst. Mater.* **221**, 15 (2006).
- [43] M. I. Aroyo, A. Kirov, C. Capillas, J. M. Perez-Mato, and H. Wondratschek, Bilbao Crystallographic Server: II. Representations of crystallographic point groups and space groups, *Acta Crystallogr. A* **62**, 115 (2006).